Nanoscale

PAPER

View Article Online
View Journal | View Issue

Check for updates

Cite this: *Nanoscale*, 2020, **12**, 21923

A structure and activity relationship for single-walled carbon nanotube growth confirmed by *in situ* observations and modeling†

Hsin-Yun Chao,[a,b] Hua Jiang,[c] Francisco Ospina-Acevedo,[d] Perla B. Balbuena,[d] Esko I. Kauppinen,[c] John Cumings[a] and Renu Sharma *[b]

Received 12th August 2020,
Accepted 3rd October 2020

DOI: 10.1039/d0nr05916a

rsc.li/nanoscale

The structure and phase transformation of a cobalt (Co) catalyst, during single walled carbon nanotube (SWCNT) growth, is elucidated for inactive, active and deactivated nanoparticles by *in situ* imaging using an environmental transmission electron microscope. During nanotube growth, the structure was analyzed using Miller indices to determine the types of planes that favor anchoring or liftoff of nanotubes from the Co catalyst. Density functional theory was further applied to model the catalyst interactions to compare the work of adhesion of the catalyst's faceted planes to understand the interactions of different Miller planes with the graphene structure. Through in-depth studies of multiple distinct Co nanoparticles, we established a dominant nanoparticle phase for SWCNT growth. In addition, we identified the preferred lattice planes and a threshold for work of adhesion to allow the anchoring and liftoff of SWCNTs.

Introduction

After nearly three decades since their emergence, carbon nanotubes (CNTs), in particular single-walled carbon nanotubes (SWCNTs), have still remained one of the most promising nanomaterials for future applications in nanotechnology.[1] Their appealing electronic properties rely critically on their unique chiral structure at the atomic scale.[2] One major barrier in developing SWCNT-based nanoelectronics is to selectively obtain desirable structural characteristics such as diameter and chirality. In contrast to post-synthesis chirality-separation processes, which are usually complex, costly, and destructive, direct control of the SWCNT structure during growth is highly preferred.[3] Among a wide selection of synthesis methods, catalytic chemical vapor deposition (C-CVD) is believed to be the one that offers the most promise for such control and bids a laboratory to large scale production. Currently, it has been widely used in a great number of attempts for selective growth of SWCNTs with a single chirality,[4,5] or predefined chirality,[6] or with uniform electrical properties (metallic or semi-conducting nanotubes).[3,7]

Despite tremendous pioneering efforts in the past, a lack of full understanding of the SWCNT growth mechanisms has largely hindered the paths towards the controlled growth of carbon nanotubes. A typical C-CVD process usually involves the high-temperature decomposition of carbon-containing molecules on catalyst nanoparticles (typically using transition metal catalysts like Fe, Co, Ni, *etc.*), followed by nucleation and growth of carbon nanotubes. Obviously, the catalyst nanoparticles play a central role, acting as templates for the nucleation of initial carbon caps that eventually determine the chiral structure of carbon nanotubes.[8–10] Recent experimental observations[10–13] have suggested that the chiral-selective growth likely follows the vapor–solid–solid (VSS) growth mode, where the catalyst nanoparticles stay in the crystalline state rather than the liquid state. It is generally believed that the diameters of the nanotubes are strongly correlated with those of the nanoparticles, but in reality, the growth can proceed with either tangential or perpendicular modes,[14,15] depending on the chosen catalysts as well as specific growth conditions, including carbon precursors, pressure, temperature, *etc.*[16] Therefore, the precise catalyst–nanotube relationship remains unclear, and insights into atomic information of the catalyst dynamics from the nucleation to cap formation are certainly needed.

Environmental transmission electron microscopy (ETEM) is a powerful tool for investigating the atomistic dynamical growth mechanism in terms of morphology and crystal struc-

[a]*Materials Science and Engineering, University of Maryland, College Park, MD, USA*
[b]*Physical Measurement Laboratory, National Institute of Standards and Technology, Gaithersburg, MD, USA. E-mail: renu.sharma@nist.gov*
[c]*Department of Applied Physics, Aalto University School of Science, P.O. Box 15100, FI-00076 Aalto, Finland*
[d]*Artie McFerrin Department of Chemical Engineering, Texas A&M University, College Station, TX, USA*

†Electronic supplementary information (ESI) available. See DOI: 10.1039/d0nr05916a

Published on 05 October 2020. Downloaded by National Institutes of Standards & Technology on 11/5/2020 6:16:33 PM.

This journal is © The Royal Society of Chemistry 2020

Published on 05 October 2020. Downloaded by National Institutes of Standards & Technology on 11/5/2020 6:16:33 PM.

ture, as well as elemental compositions.[17–19] In recent years, it has been actively employed to observe a number of C-CVD processes to investigate the initial stage for SWCNT growth. In a succession of work, both Picher *et al.*[13] and Rao *et al.*[10] have independently shown that the nucleation of a carbon nanotube begins with the formation of a graphene embryo that progressively lifts off to convert into a tubular structure. The difference in works of adhesion of adjacent facets of the catalyst nanoparticles has been proposed to account for the conversion.[13] This provides a reasonable foundation to explain an early study by He *et al.*[20] where they report highly preferential growth of semiconducting SWCNTs with an exceptionally large population of (6,5) tubes grown on Co nanoparticles with a well-defined crystal structure. Interestingly, Zhang *et al.*[12] observed multiple nucleation of nanocarbon caps from the same catalyst nanoparticles. On the other hand, structural fluctuations[21] and morphology evolution[22] in catalytic nanoparticles during growth processes have also been observed, which can influence the catalytic outcomes.

It has been widely recognized that transition metal catalysts (Fe, Co or Ni) undergo a phase transition to form metal carbide phases prior to catalyzing CNT growth.[10,13,18,23] However, no prior studies statistically analyze the crystal structures during this nanoparticle evolution through different phases, and no prior studies have correlated these phases with their catalytic performance for SWCNT growth.

Modeling nanoscale interactions is also crucial for in-depth understanding of the mechanisms driving the experimental observations. Understanding the interplay of the catalyst structure and nanotube growth has previously benefited from density functional theory (DFT) calculations.[13,24] Incorporating the nanoparticle structure and terminations, DFT-based dynamics allows observation of structural fluctuations. DFT structural optimization also contributes to the characterization of interfacial properties such as work of adhesion.

In this work, by employing ETEM imaging as an experimental platform, we are able to observe atomic-resolution dynamic structural evolution of catalytic nanoparticles in real time. We have obtained a sizable dataset for statistical analysis with respect to the types of catalyst structures that promote or inhibit the growth. We distinguish between active, inactive, and deactivated Co-based nanoparticles. We show that the ability for nanotube growth depends on both the catalyst phase and the faceted planes of the catalyst surface. In addition, we propose that the work of adhesion between the nanotube and catalyst interface, as predicted by DFT calculations, plays a critical role in the determination of the growth.

Experimental and modeling methods

Materials and methods

A powder of the Co/Mo catalyst on the MgO support, provided by Prof. Zafar Iqbal,[25] is used for the single-walled nanotube growth by the C-CVD method using acetylene (C_2H_2) as the carbon precursor. A suspension of catalyst powder in isopropyl alcohol was ultrasonicated and subsequently drop-cast onto a 5 μm by 30 μm silicon nitride membrane chip, with a squared array of 3 by 15 holes 0.8 μm in width with a 1.1 μm pitch size patterned on the silicon nitride membranes using a focused ion beam (FIB) and compatible with a micro-electromechanical system (MEMS) heating holder, capable of reaching up to 1100 °C. Catalyst support regions around the holes allow for observing nanotube growth unobstructed by the support film. The sample holder is then inserted into an ETEM equipped with a monochromated 80 keV to 300 keV Schottky field emission electron gun, an image corrector, and pressure limiting apertures. The ETEM is capable of maintaining gas pressures up to 2×10^3 Pa in the specimen chamber. For our experiments, the electron gun is set at 80 keV to minimize electron knock-on damage to the nanotube wall structure. The sample is first heated in 300 Pa of oxygen for 30 minutes at 900 °C to burn off residual carbon contaminants. C_2H_2 is used as the carbon feedstock at low pressures ranging from 0.02 Pa to 0.005 Pa for controlled growth and maintaining atomic resolution.[13] Temperatures range from 700 °C to 900 °C. High resolution TEM (HRTEM) images and movies were recorded at a rate of 15 frames per second using a charge-coupled device (CCD) to capture structural and morphological changes in the Co catalyst nanoparticles in real-time during SWCNT nucleation and growth.

The chemical composition of the catalyst sample is characterized using electron energy loss spectroscopy (EELS). HRTEM images and frames extracted from movies are analyzed using Fast Fourier Transform (FFT) to determine the *d*-spacings and angles of the crystal structure and associated faceted planes. CrystalBall, a custom algorithm formulated by Mazzucco *et al.* at the National Institute of Standards and Technology (NIST), is used for unambiguous structure determination.[26] Additional information is provided in the ESI† for determining the matching structure and an example is provided in ESI Table S2.† The crystallography data for Co_2C and Co_3C *d*-spacings and angles of lattice planes ($h\ k\ l$) are obtained from the literature[27–29] for reference.

Computational methods

DFT calculations are used to determine the work of adhesion (W_{adh}) for comparison and modeling of the interactions between the faceted planes and the graphene film. Surface energies of Co_2C and Co_3C obtained from DFT are reported in ESI, Fig. S2 and S3,† respectively. For these calculations, the bulk crystal structures of Co_2C and Co_3C are obtained from the literature.[27–29] These Co_2C and Co_3C structures are optimized using DFT to obtain their lattice constants varying possible degrees of freedom dependent on the cell shape, volume, and atomic positions.[30] A graphene film is placed at an initial distance from the carbide surface calculated from preliminary simulations to allow for observations of interactions between the catalyst and graphene. The initial distances and detailed procedures are included in the ESI (Fig. S4 and Table S6†). The supercell dimensions are defined according to the graphene layer area to make sure that the graphene is a finite layer that

 This journal is © The Royal Society of Chemistry 2020

Published on 05 October 2020. Downloaded by National Institutes of Standards & Technology on 11/5/2020 6:16:33 PM.

does not interact with its periodic images created due to periodic boundary conditions. All simulations are carried out using the Vienna *Ab initio* Simulation Package (VASP)[31–34] with projector augmented wave (PAW) pseudopotential[35,36] for the core electrons, and a plane-wave basis set is implemented with a cutoff energy of 400 eV for the valence electrons.

The Perdew-Burke-Ernzerhoff (PBE) functional[37,38] is used to describe the electron exchange and correlation between the supercell lattice and graphene layer. For partial occupancies, the Methfessel–Paxton method[39] with an order of two and a sigma value of 0.2 eV is utilized. In addition, spin polarization is considered in all simulations and a 4 by 4 by 1 *k*-point Monkhorst–Pack mesh[40] sampling is employed on the surface of the Brillouin zone for energy minimization. Furthermore, the convergence criteria for the electronic self-consistent loop are set to be 10^{-4} eV and 10^{-3} eV for atomic relaxation.

Results and discussion

An EELS map of the sample, acquired at room temperature under vacuum after heating in oxygen (ESI Fig. S1†), shows the presence of CoO particles on the MgO support. The chemical state of Co particles was determined by comparing positions of L3 and L2 peaks with reported values (Table S1†).[41] As reported earlier, Mo is not found in the catalyst nanoparticles and is most likely dispersed in the catalyst support.[13] Also, CoO nanoparticles are reported to reduce to Co metal upon heating in the C_2H_2 environment before carburizing to Co_2C or Co_3C.[13] Initial ETEM observations show that catalyst nanoparticles become clearly visible on the MgO support at elevated temperatures of 700 °C to 900 °C; thus it is possible to track the structural evolution of the catalyst nanoparticles and the later growth progress on catalyst sites. It is noteworthy that the catalyst sample contains a number of nanoparticles. However, not all particles are catalytically active enough for lowering the energy barrier to initiate the growth. Therefore, we use the term catalyst to denote a nanoparticle that has the potential for lowering the energy barrier. ESI Movie S1† demonstrates that most catalyst nanoparticles of diameters varying from 1 nm to 5 nm start to grow CNTs at different rates in the beginning, then slow down or stop completely with time. Initially, nanoparticles labeled 1 through 5 show graphene film formation as well as many other nanoparticles (Movie S1†). After ≈18 seconds, nanoparticles 2, 3, and 4 become active and liftoff of the graphene film and SWCNT growth are observed, while nanoparticles 1 and 5 remain inactive and encapsulated by the graphene film even with extended observation time. There are also many other catalysts actively growing SWCNTs at various stages of growth and rates that vary widely even from catalyst nanoparticles with a similar size. The difference in the linear growth rate may be controlled by the chirality of the tube, which may in turn depend on the catalyst facets.[42,43] However, the vibrations and movement of the tubes during growth kept us from *in situ* measurements of chirality.

Based on statistical observations of 43 rounds of experiments and 143 movie data, we observe three broad types of catalyst nanoparticles: active, inactive and deactivated, as seen in Movies S2–S4,† respectively, and the extracted HRTEM images (Fig. 1). For active nanoparticles, a graphene film first forms on the surface of the catalyst during nucleation, and the film subsequently detaches from one of the centers of the nanoparticle facets, referred to as nanotube liftoff,[13] to form a SWCNT (Fig. 1a). Inactive nanoparticles can either be encapsulated by the graphene film such as nanoparticles 1 and 5 in Movie S1† or have no graphene layer formation (Fig. 1b). The catalyst nanoparticles that show no nanotube growth (no liftoff) even after the formation of a graphene film are considered inactive for SWCNT growth. Finally, SWCNTs may either stop growing for a short period of time or may stop with no additional growth within the observation period, which we denote as deactivated (Fig. 1c). The active catalyst nanoparticles were observed to become deactivated, given enough time.

Atomic structures of the three types of nanoparticles were deduced by measuring the lattice spacing from FFTs (insets in the bottom right-hand corner) of the images shown in Fig. 1. The FFTs are critical for the determination of the nanoparticle structure, orientation and indices of surface facets. Co_2C and Co_3C carbide phases are both orthorhombic crystal systems but with different lattice constants and space groups. The active catalyst shows nanotube growth with time and has the Co_2C structure (Fig. 1a). Inactive nanoparticles do not exhibit growth despite being in an environment conducive to SWCNT growth for other nanoparticles and are found to have the Co_3C structure (Fig. 1b). Finally, the deactivated nanoparticle, also with the Co_3C structure, had initial liftoff, but no further growth. In general, we find that the nanoparticles in the Co_2C phase favor nucleation and growth of SWCNTs. The live FFTs indicate that the nanoparticle structure may fluctuate with time, which could either indicate a change of phase or simply nanoparticle rotation resulting in shifting of the zone axis. In the case of the nanoparticles in Fig. 1, the dominant phases remain the same during the period of observation, but there is shifting in the zone axis.

Statistical observations show that inactive nanoparticles can be further categorized into two types: non-encapsulated and encapsulated. Non-encapsulated nanoparticles do not have any graphene film formation, while encapsulated nanoparticles have a graphene film form, which, however, does not liftoff to form a tubular structure. Fig. 2a shows an example of an encapsulated nanoparticle of 3 nm in diameter that is covered with a graphene layer without liftoff. The structure of the nanoparticle, as determined by FFT analysis (inset), is Co_3C with the graphene adhering to the (022), (211), and $(\bar{2}11)$ faceted planes. It has been reported that Co-terminated planes are optimal for anchoring;[13] thus we make the argument that the encapsulated nanoparticles have uniformly Co-terminated faceted planes. Nanoparticles in Fig. 2b have the same Co_3C structure of similar size with faceted planes of (111), (020), and $(1\bar{1}1)$, but show no preliminary graphene layer. Conversely,

Published on 05 October 2020. Downloaded by National Institutes of Standards & Technology on 11/5/2020 6:16:33 PM.

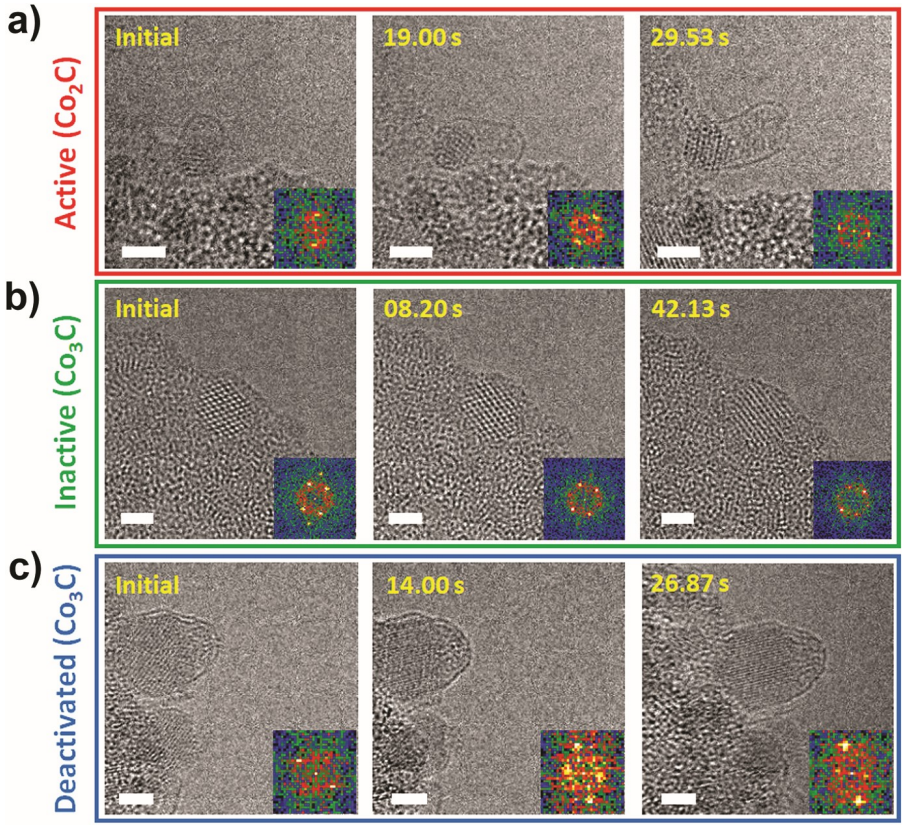

Fig. 1 Time-resolved HRTEM images for (a) active, (b) inactive, and (c) deactivated nanoparticles. Scale bars represent 2 nm. Insets are FFT of the nanoparticles. HRTEM images extracted from ESI Movies S2–S4† for active, inactive, and deactivated nanoparticles, respectively.

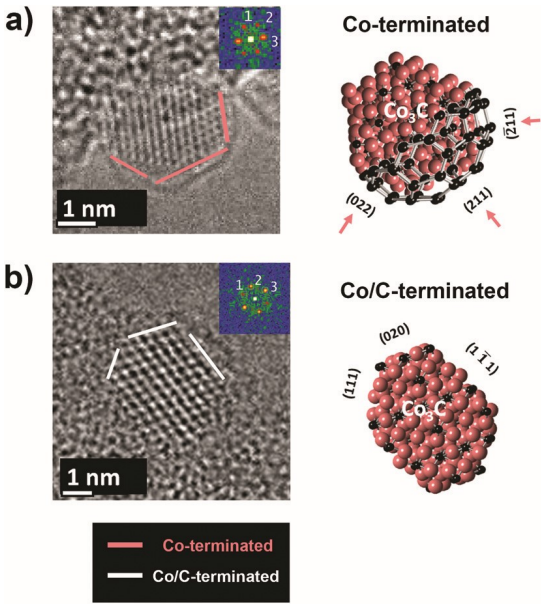

Fig. 2 *In situ* ETEM images of two types of inactive nanoparticles with associated fast Fourier transforms in the insets. Models of the surface terminations are to the right of the images. Faceted planes are labeled with the associated nanoparticle phases. (a) Is a nanoparticle encapsulated by a graphene film without liftoff, while (b) is a case where no graphene layer is formed.

these faceted planes are most likely Co/C terminated, where the graphene layer is unable to attach to the nanoparticle surface. Models for the respective structures are displayed on the right of each nanoparticle image to illustrate the structure and surface facets.

Examples of active catalyst structures are shown in Fig. 3. The FFT analysis shows that both nanoparticles are in the Co_2C phase which leads to the growth of carbon nanotubes. For the nanoparticle shown in Fig. 3a, the anchoring planes were determined to be $(01\bar{1})$ and $(0\bar{1}\bar{1})$, while the liftoff plane for CNT growth is (020). In contrast to the short nanotube in Fig. 3a, considered to be at the initial stages of growth, Fig. 3b shows a longer nanotube, possibly at the later stages of growth. For the latter case, the anchoring planes are $(1\bar{1}0)$ and (110) with (020) as the liftoff plane. These cases demonstrate that the active lift-off of the SWCNT occurs from (020) faceted planes and the SWCNT anchors on the {011} and {110} family of planes regardless of its stage in growth.

Fig. 4 shows a series of time-resolved images extracted from a movie (Movie S5†) which illustrates the deactivation process. The graphene cap initiates on the surface of the nanoparticle of the Co_2C structure determined by FFT analysis (Fig. 4a). The faceted planes whereupon the graphene is adhering are (111), (020), and $(\bar{1}1\bar{1})$. After 10 s, the catalyst initiates the formation of a carbon cage on its surface. The nanoparticle morphology was observed to change by shifting the facet planes while

 This journal is © The Royal Society of Chemistry 2020

Published on 05 October 2020. Downloaded by National Institutes of Standards & Technology on 11/5/2020 6:16:33 PM.

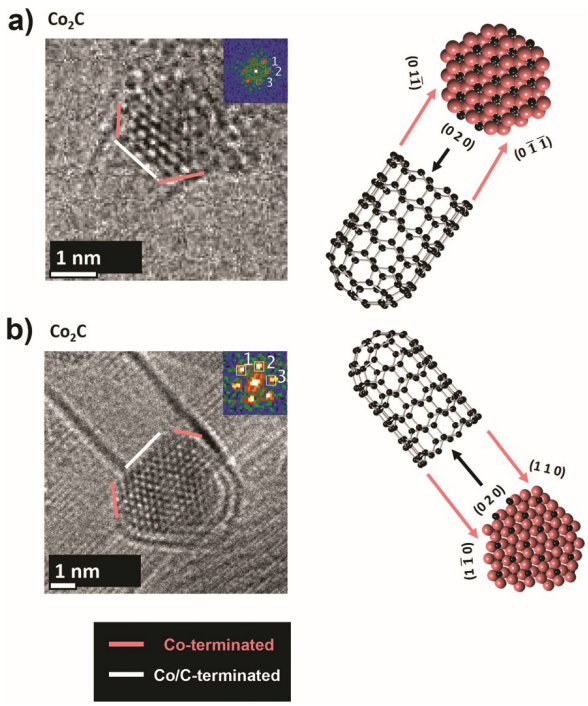

Fig. 3 Two different cases of active nanoparticles during SWCNT growth. Catalyst (a) has anchoring planes of (0 1 1̄), (0 1̄ 1̄) and liftoff plane of (0 2 0), while catalyst (b) has anchoring planes of (1 1̄ 0), (1 1 0) and lift-off plane of (0 2 0).

maintaining a Co_2C catalyst structure as determined from FFT's inset in the lower right-hand corner (Fig. 4b). The apparent size change is attributed to orientation change as particles are not perfect spheres. The anchoring planes are determined to be (011), while the liftoff plane is (0$\bar{1}$1). Subsequently, CNT growth termination occurs after around 10 s from liftoff with no further growth (Fig. 4c). At this point, the nanoparticle structure changed from Co_2C to Co_3C and the faceted planes are identified as (20$\bar{1}$), (002), and (201). As reported earlier, structural fluctuations can be attributed to carbon incorporation and depletion during non-equilibrium conditions of SWCNT growth.[21]

Fig. 5 shows statistical results of a total of 24 distinct cobalt carbide nanoparticles at varying stages of their activities for growing carbon nanotubes. The data show that all the active catalysts measured have the Co_2C dominant phase (Fig. 5a). Nanoparticles in the Co_3C dominant phase are either inactive or deactivated. For the 11 active catalysts in the Co_2C dominant phase, we observe that there is a distinct difference in the type of plane for anchoring and liftoff (Fig. 5b). The Miller indices for the anchoring planes, where the graphene film attaches, are in the {111}, {110}, {101}, or {011} family, whereas for the liftoff planes, where the graphene film detaches from the catalyst surface to form the nanotube, the Miller indices are in the {200}, {020}, and {002} family. These findings demonstrate that the growth prefers certain types of planes, and particularly, catalysts may have to be favorably oriented to enable the

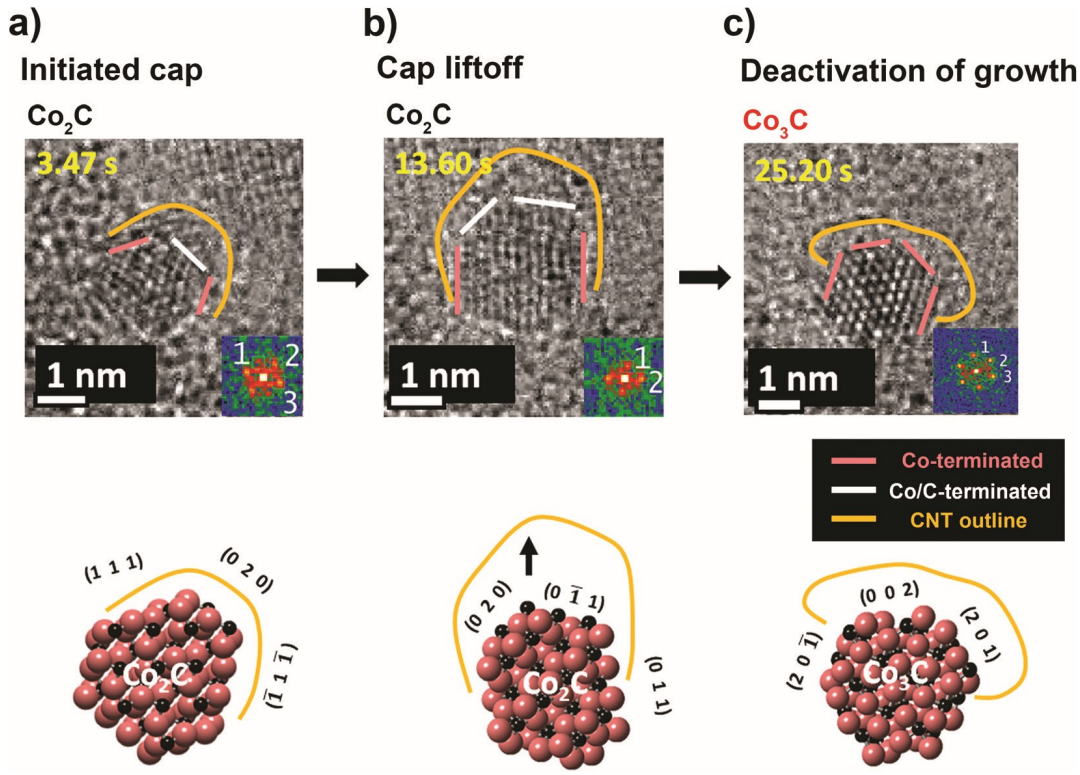

Fig. 4 Sequential images demonstrating the nanoparticle deactivation process. (a) Initial cap formation from the catalyst particle of the Co_2C phase; (b) liftoff; and (c) final deactivation with a transition of the nanoparticle from the original Co_2C phase to the Co_3C phase.

Published on 05 October 2020. Downloaded by National Institutes of Standards & Technology on 11/5/2020 6:16:33 PM.

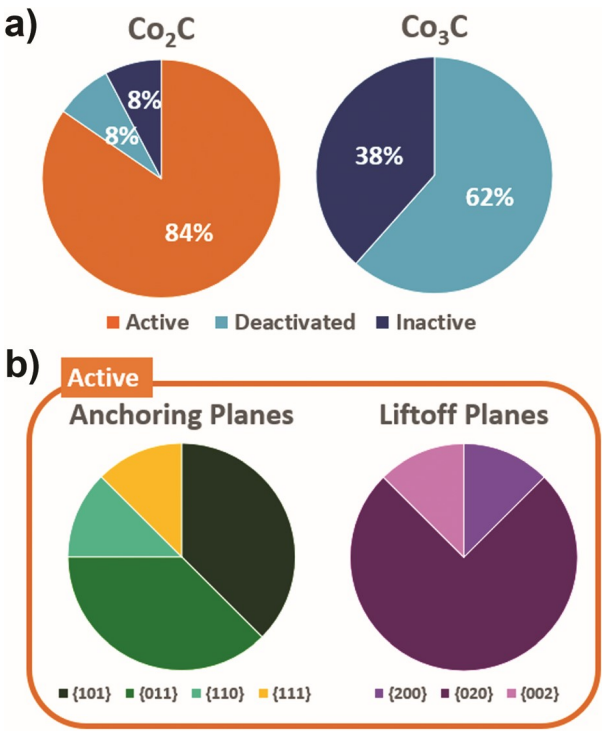

Fig. 5 Analyzed result of nanoparticles. (a) shows the percentages of phases that are active, deactivated, and inactive, while (b) shows the planes for anchoring and liftoff for the active catalysts in the Co_2C phase.

growth. Systematically tabulated results of all active, deactivated, and inactive nanoparticles measured are included in ESI Tables S3–S5,† respectively. The possible error has a median of 3.43% and 3.86% for the *d*-spacings and angles, respectively.

From these data, we infer that the phase transition from Co_2C to Co_3C appears to deactivate nanoparticles, but there are certain cases where the inactive nanoparticles remain in the Co_2C phase. Therefore, we want to further explore the mechanisms at work using DFT calculations combined with the measured Miller indices of the faceted planes. We theorize that the difference in the activity of nanoparticles for SWCNT growth is determined by the work of adhesion between the graphene film and nanoparticle structural facets that was further investigated using DFT calculations. The work of adhesion (W_{adh}) between the faceted planes of the nanoparticle structure and the graphene film is given by:[44]

$$W_{adh} = \frac{E_{Co_2C+graph} - (E_{Co_2C} + E_{graph})}{Area}$$

The equation above denotes that the combined energy of Co_2C and graphene ($E_{Co_2C+graph}$) subtracted by the sum of the energies of Co_2C (E_{Co_2C}) and graphene (E_{graph}) separately per area is equal to the W_{adh}. Using these DFT data, we can correlate the nanoparticle changes from our experiments with computational calculations.

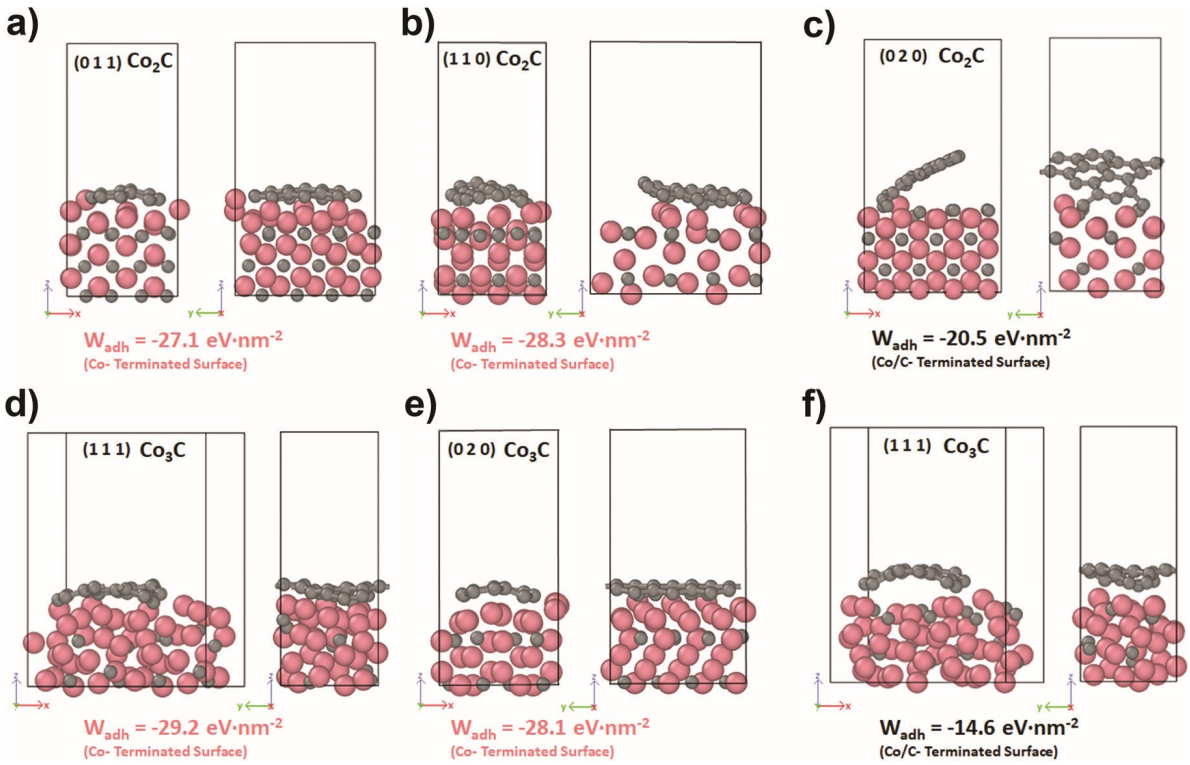

Fig. 6 Tableau showing the final DFT calculations between the graphene layer and nanoparticles in carbide form with front and side views. Top row phases are Co_2C and bottom row phases are Co_3C. For the cobalt-terminated surface (a), (b), (d) and (e), the interaction planes are (0 1 1), (1 1 0), (1 1 1) and (0 2 0), respectively. For cobalt and carbon-terminated nanoparticles (c) and (f), the interaction planes are (0 2 0) and (1 1 1), respectively. The W_{adh} is noted below each case.

 This journal is © The Royal Society of Chemistry 2020

Published on 05 October 2020. Downloaded by National Institutes of Standards & Technology on 11/5/2020 6:16:33 PM.

We employ DFT to calculate the W_{adh} for active, inactive, and deactivated nanoparticles based on surface chemistry (denoted by carbon terminations, metal terminations, or a combination of both) and surface structure (*i.e.* faceted planes). Varying surface chemistry and structure gives way to an array of different W_{adh}, with pertinent examples shown in Fig. 6. Detailed information about the computational methods to calculate the W_{adh} and the surfaces evaluated can be found in the ESI (Table S7†). These simulations demonstrate that the interaction at the interface of the nanoparticle and the graphene film after equilibrium is reached. One observed trend is that the W_{adh} is strongly negative (below −23 eV nm^{-2}) for Co-terminated surfaces (Fig. 6a, b, d, e) compared to the Co/C-terminated surfaces (Fig. 6c and f). Additionally, conformality of the graphene film is greatly improved, which is optimal for the Co-terminated surface. For the Co/C-terminated surface, graphene shows detachment and poor conformality. This confirms the above assertions that Co-terminated surfaces are preferred for graphene anchoring, while Co/C-terminated surfaces for liftoff.[13] Among all calculated planes, it is observed that the minimum threshold value of W_{adh}, above which liftoff occurs, is −23 ± 2 eV nm^{-2}. As seen in Table 1, calculated planes correlate with this threshold in terms of Co and Co/C-terminations.

Table 1 The average work of adhesion associated with each type of faceted surface for Co_2C and Co_3C nanoparticle phases for Co and Co/C terminations. W_{adh} values in units of eV nm^{-2}

	Co_2C				Co_3C	
Faceted surface	(020)	(101)	(011)	(110)	(020)	(111)
W_{adh} for Co-terminated	−26.8	−25.5	−27.1	−28.3	−25.7	−29.2
W_{adh} for Co/C-terminated	−20.5	−14.3	−10.7	−7.4	−10.8	−18.4

Neither the experimental data nor DFT calculations could pinpoint the forces that influence the surface termination of various facets in nanoparticles as it is complicated by the interaction with the substrate as well as with adsorbed gas molecules.[45,46] However, a relationship between the surface termination and SWCNT growth can be drawn by comparing the experimental results and calculated W_{adh} for active, inactive, and deactivated nanoparticles, (Fig. 2–4). For the encapsulated nanoparticle, we postulate that a Co-terminated plane with uniform W_{adh} at all facets leads to the growth of a graphene layer, but no liftoff produces a SWCNT due to the lack of disparity in W_{adh} between adjacent facets (Fig. 2a). This also explains the small percentage of deactivated or inactive nanoparticles found to be in the Co_2C phase. Even though in a carbon-rich Co_2C phase, a similar W_{adh} between adjacent faceted planes could prove detrimental for SWCNT growth.

Active catalysts are those observed to have planes with a larger difference in W_{adh}. The nanoparticle in Fig. 3a has anchoring planes in the {011} family with a (020) liftoff plane. As discussed previously, we notice that the anchoring planes are most likely Co-terminated, where W_{adh} = −27.1 eV nm^{-2}, while the liftoff plane is a Co/C-terminated plane with W_{adh} = −20.5 eV nm^{-2}. Similarly, the nanoparticle in Fig. 3b has anchoring planes in the Co-terminated {110} family with W_{adh} = −28.3 eV nm^{-2} and a Co/C-terminated (020) liftoff plane with W_{adh} = −20.5 eV nm^{-2} (Table 1). Both examples show that

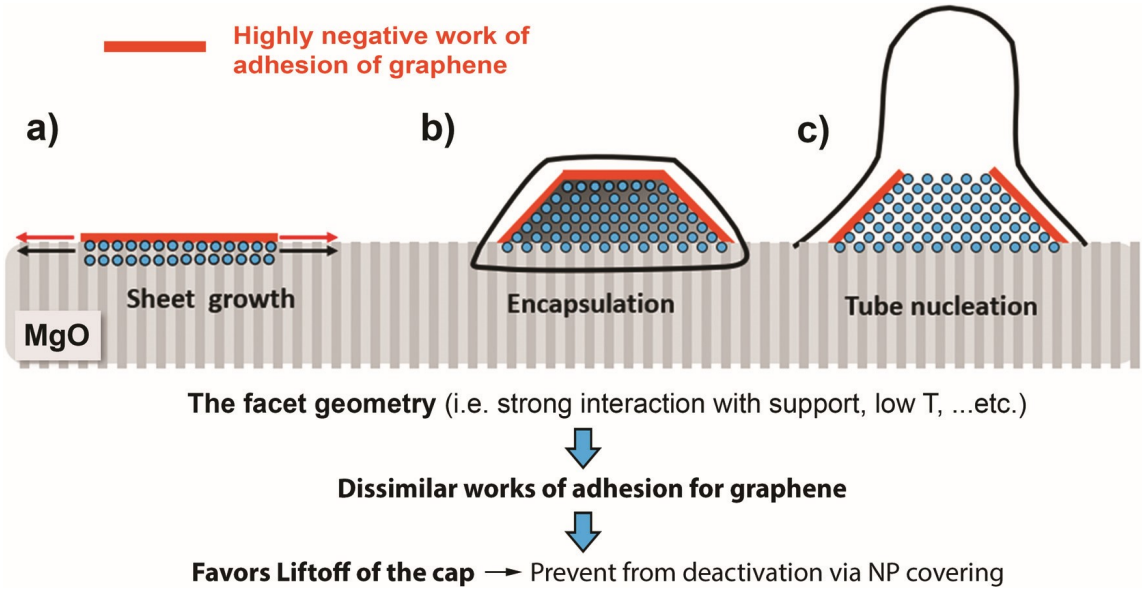

Fig. 7 This diagram shows the growth mechanism of SWCNT. (a) In the first case on the left, linear sheet growth occurs due to the lack of faceted geometry. (b) In the second case, encapsulation occurs due to the similar W_{adh} between adjacent planes. (c) The last case demonstrates a successful liftoff of the SWCNT, which is closely related to the faceted geometry of the nanoparticle and the W_{adh} between the faceted nanoparticle surface relative to the graphene.

Published on 05 October 2020. Downloaded by National Institutes of Standards & Technology on 11/5/2020 6:16:33 PM.

faceted planes with a highly negative W_{adh} below −23 eV nm^{-2} provide an anchoring plane for the SWCNT, whereas the liftoff plane has a lower negative W_{adh} above −23 eV nm^{-2}. This trend persists for other active catalysts measured.

Initial liftoff of the SWCNT (Fig. 4a) with the faceted planes shows a difference in W_{adh} correlating with the previously discussed characteristics of an active catalyst (Fig. 3). Next, the liftoff occurs where it remains in the Co_2C phase, but the faceted planes are transformed to a (011) anchoring plane and $(0\bar{1}1)$ liftoff plane (Fig. 4b). We postulate that this is to accommodate for a higher difference in W_{adh} where the anchoring plane is Co-terminated with W_{adh} = −27.1 eV nm^{-2}, while the Co/C-terminated liftoff plane has W_{adh} = −10.7 eV nm^{-2}. This disparity in W_{adh} enables the liftoff of the nanotubes. After deactivation, the nanoparticle transitions into the Co_3C phase and SWCNT growth is terminated. In addition to a phase transformation, the faceted planes most likely transition into uniformly Co-terminated planes, preventing further nanotube propagation and minimizing the difference of W_{adh} between adjacent planes.

Subsequently, the growth mechanism based on W_{adh} can be formulated. A synopsis of our data is visualized with the diagram in Fig. 7. A faceted rather than planar geometry is critical for preventing parallel sheet growth of graphene (Fig. 7a). For a faceted nanoparticle, if the W_{adh} is uniformly low for all adjacent planes, encapsulation of the nanoparticle might occur inhibiting further growth (Fig. 7b). If there is a disparity in W_{adh} between the different faceted planes, it then creates a favorable condition for liftoff (Fig. 7c).

Conclusions

In this work, we have investigated real-time dynamic structural evolution of catalytic nanoparticles at the atomic scale by *in situ* observation of the growth of SWCNTs using an ETEM. We find that the growth and termination of the SWCNT directly correlate with the dominant phase and faceted planes of the nanoparticles. Nanoparticles of the carbon-rich Co_2C phase, as previously reported for the Fe catalyst,[47] are favorable for the growth, while those of the Co_3C phase are observed to be inactive or deactivated in general. Moreover, preferable planes for either anchoring or liftoff during active growth are determined through analyzing the surface termination of nanoparticle facets *via* FFT. After the deactivation of the nanoparticles, the associated faceted planes do not demonstrate preferable planes.

For insights into the understanding of the interplay between the nanoparticle structural evolution and the nanotube growth, we have conducted DFT calculations based on the surface free energy of the carbide nanoparticle and the graphene film. It is demonstrated that the W_{adh} of adjacent faceted planes of the catalyst nanoparticle plays a critical role in the interfacial interactions between the catalyst and the graphene film during anchoring and liftoff for forming SWCNTs. It also determines whether the growth will either initiate, continue or terminate. A difference in the W_{adh} is necessary to enable liftoff and the subsequent propagation of the nanotube. Otherwise encapsulation or stoppage of the growth will occur. Since W_{adh} is relevant for all types of catalytic growth, we suggest that this growth mechanism model can be further applied to other systems involving catalytic growth, including other VSS-grown materials similar to SWCNTs.

Disclaimer

Certain commercial equipment, instruments, or materials are identified in this paper in order to specify the experimental procedure adequately. Such identification is not intended to imply recommendation or endorsement by the National Institute of Standards and Technology, nor is it intended to imply that the materials or equipment identified are necessarily the best available for the purpose.

Conflicts of interest

There are no conflicts to declare.

Acknowledgements

H. C. acknowledges support under the Cooperative Research Agreement between the University of Maryland and the National Institute of Standards and Technology Physical Measurement Laboratory, award 70NANB14H209, through the University of Maryland.

Notes and references

1 G. Hills, C. Lau, A. Wright, S. Fuller, M. D. Bishop, T. Srimani, P. Kanhaiya, R. Ho, A. Amer, Y. Stein, D. Murphy, Arvind, A. Chandrakasan and M. M. Shulaker, *Nature*, 2019, **572**, 595–602.
2 N. Hamada, S. I. Sawada and A. Oshiyama, *Phys. Rev. Lett.*, 1992, **68**, 1579–1581.
3 C. Liu and H. M. Cheng, *J. Am. Chem. Soc.*, 2016, **138**, 6690–6698.
4 Y. Li, C. Y. Xu, J. Y. Wang and L. Zhen, *Sci. Rep.*, 2014, **4**, 1–8.
5 S. Zhang, L. Kang, X. Wang, L. Tong, L. Yang, Z. Wang, K. Qi, S. Deng, Q. Li, X. Bai, F. Ding and J. Zhang, *Nature*, 2017, **543**, 234–238.
6 J. Liu, C. Wang, X. Tu, B. Liu, L. Chen, M. Zheng and C. Zhou, *Nat. Commun.*, 2012, **3**, 1–7.
7 Z. Zhu, N. Wei, W. Cheng, B. Shen, S. Sun, J. Gao, Q. Wen, R. Zhang, J. Xu, Y. Wang and F. Wei, *Nat. Commun.*, 2019, **10**, 1–8.
8 S. Reich, L. Li and J. Robertson, *Phys. Status Solidi B*, 2006, **243**, 3494–3499.

 This journal is © The Royal Society of Chemistry 2020

Published on 05 October 2020. Downloaded by National Institutes of Standards & Technology on 11/5/2020 6:16:33 PM.

9 H. Zhu, K. Suenaga, A. Hashimoto, K. Urita, K. Hata and S. Iijima, *Small*, 2005, **1**, 1180–1183.
10 R. Rao, R. Sharma, F. Abild-Pedersen, J. K. Nørskov and A. R. Harutyunyan, *Sci. Rep.*, 2014, **3**, 1–6.
11 F. Yang, X. Wang, D. Zhang, J. Yang, D. Luo, Z. Xu, J. Wei, J. Q. Wang, Z. Xu, F. Peng, X. Li, R. Li, Y. Li, M. Li, X. Bai, F. Ding and Y. Li, *Nature*, 2014, **510**, 522–524.
12 L. Zhang, M. He, T. W. Hansen, J. Kling, H. Jiang, E. I. Kauppinen, A. Loiseau and J. B. Wagner, *ACS Nano*, 2017, **11**, 4483–4493.
13 M. Picher, P. A. Lin, J. L. Gomez-Ballesteros, P. B. Balbuena and R. Sharma, *Nano Lett.*, 2014, **14**, 6104–6108.
14 M. F. C. Fiawoo, A. M. Bonnot, H. Amara, C. Bichara, J. Thibault-Pénisson and A. Loiseau, *Phys. Rev. Lett.*, 2012, **108**, 1–5.
15 Y. Magnin, H. Amara, F. Ducastelle, A. Loiseau and C. Bichara, *Science*, 2018, **362**, 212–215.
16 M. He, Y. Magnin, H. Jiang, H. Amara, E. I. Kauppinen, A. Loiseau and C. Bichara, *Nanoscale*, 2018, **10**, 6744–6750.
17 S. Helveg, C. López-Cartes, J. Sehested, P. L. Hansen, B. S. Clausen, J. R. Rostrup-Nielsen, F. Abild-Pedersen and J. K. Nørskov, *Nature*, 2004, **427**, 426–429.
18 H. Yoshida, S. Takeda, T. Uchiyama, H. Kohno and Y. Homma, *Nano Lett.*, 2008, **8**, 2082–2086.
19 J. Winterstein and R. Sharma, in *Controlled Atmosphere Transmission Electron Microscopy*, ed. T. W. Hansen and J. B. Wagner, Springer, 2016, pp. 213–235.
20 M. He, H. Jiang, B. Liu, P. V. Fedotov, A. I. Chernov, E. D. Obraztsova, F. Cavalca, J. B. Wagner, T. W. Hansen, I. V. Anoshkin, E. A. Obraztsova, A. V. Belkin, E. Sairanen, A. G. Nasibulin, J. Lehtonen and E. I. Kauppinen, *Sci. Rep.*, 2013, **3**, 1–7.
21 P. A. Lin, J. L. Gomez-Ballesteros, J. C. Burgos, P. B. Balbuena, B. Natarajan and R. Sharma, *J. Catal.*, 2017, **349**, 149–155.
22 P. Ann Lin, B. Natarajan, M. Zwolak and R. Sharma, *Nanoscale*, 2018, **10**, 4528–4537.
23 R. Sharma, E. Moore, P. Rez and M. M. J. Treacy, *Nano Lett.*, 2009, **9**, 689–694.
24 Y. H. Zhao, H. Y. Su, K. Sun, J. Liu and W. X. Li, *Surf. Sci.*, 2012, **606**, 598–604.
25 A. Goyal, D. A. Wiegand, F. J. Owens and Z. Iqbal, *Chem. Phys. Lett.*, 2007, **442**, 365–371.
26 S. Mazzucco, M. Tanase and R. Sharma, *Crystal Ball Plus*.
27 S. Nagakura, *J. Phys. Soc. Jpn.*, 1961, **16**, 1213–1219.
28 J. Clarke and K. H. Jack, *Chem. Ind.*, 1951, **1951**, 1004–1005.
29 L. Y. Markovskii, E. T. Bezruk and G. E. Berlova, *Inorg. Mater.*, 1971, **7**, 50–52.
30 G. Kresse, M. Marsman and J. Furthmüller, *VASP the Guide*, Vienna, Austria, 2018.
31 G. Kresse and J. Hafner, *Phys. Rev. B: Condens. Matter Mater. Phys.*, 1994, **49**, 14251–14269.
32 G. Kresse and J. Hafner, *J. Non-Cryst. Solids*, 1995, **192–193**, 222–229.
33 G. Kresse and J. Furthmüller, *Phys. Rev. B: Condens. Matter Mater. Phys.*, 1996, **54**, 11169–11186.
34 G. Kresse and J. Furthmüller, *Comput. Mater. Sci.*, 1996, **6**, 15–50.
35 P. E. Blöchl, *Phys. Rev. B: Condens. Matter Mater. Phys.*, 1994, **50**, 17953–17979.
36 G. Kresse and D. Joubert, *Phys. Rev. B: Condens. Matter Mater. Phys.*, 1999, **59**, 1758–1775.
37 J. P. Perdew, K. Burke and M. Ernzerhof, *Phys. Rev. Lett.*, 1996, **77**, 3865–3868.
38 J. P. Perdew, M. Ernzerhof and K. Burke, *Phys. Rev. Lett.*, 1996, **77**, 3865–3868.
39 M. Methfessel and A. T. Paxton, *Phys. Rev. B: Condens. Matter Mater. Phys.*, 1989, **40**, 3616–3621.
40 H. J. Monkhorst and J. D. Pack, *Phys. Rev. B: Solid State*, 1976, **13**, 5188–5192.
41 Y. Zhao, T. E. Feltes, J. R. Regalbuto, R. J. Meyer and R. F. Klie, *J. Appl. Phys.*, 2010, **108**, 1–7.
42 F. Ding, A. R. Harutyunyan and B. I. Yakobson, *Proc. Natl. Acad. Sci. U. S. A.*, 2009, **106**, 2506–2509.
43 M. V. Kharlamova, C. Kramberger, Y. Sato, T. Saito, K. Suenaga, T. Pichler and H. Shiozawa, *Carbon*, 2018, **133**, 283–292.
44 S. Ebnesajjad and C. F. Ebnesajjad, in *Surface Treatment of Materials for Adhesion Bonding*, ed. S. Ebnesajjad, William Andrew Publishing, Norwich, NY, 2006, pp. XV–XVI.
45 B. Rahmani Didar and P. B. Balbuena, *Ind. Eng. Chem. Res.*, 2019, **58**, 18213–18222.
46 E. J. Lamas and P. B. Balbuena, *J. Phys. Chem. B*, 2003, **107**, 11682–11689.
47 S. Mazzucco, Y. Wang, M. Tanase, M. Picher, K. Li, Z. Wu, S. Irle and R. Sharma, *J. Catal.*, 2014, **319**, 54–60.